Current density functional framework for spin–orbit coupling: Extension to periodic systems

Yannick J. Franzke[1] and Christof Holzer[2]

[1)]*Otto Schott Institute of Materials Research, Friedrich Schiller University Jena, Löbdergraben 32, 07743 Jena, Germany*

[2)]*Institute of Theoretical Solid State Physics, Karlsruhe Institute of Technology (KIT), Wolfgang-Gaede-Straße 1, 76131 Karlsruhe, Germany*

(*Email for correspondence: christof.holzer@kit.edu)

(*Email for correspondence: yannick.franzke@uni-jena.de)

Spin–orbit coupling induces a current density in the ground state, which consequently requires a generalization for *meta*-generalized gradient approximations. That is, the exchange-correlation energy has to be constructed as an explicit functional of the current density and a generalized kinetic energy density has to be formed to satisfy theoretical constraints. Herein, we generalize our previously presented formalism of spin–orbit current density functional theory [Holzer *et al.*, J. Chem. Phys. **157**, 204102 (2022)] to non-magnetic and magnetic periodic systems of arbitrary dimension. Besides the ground-state exchange-correlation potential, analytical derivatives such as geometry gradients and stress tensors are implemented. The importance of the current density is assessed for band gaps, lattice constants, magnetic transitions, and Rashba splittings. For the latter, the impact of the current density may be larger than the deviation between different density functional approximations.

I. INTRODUCTION

In the constantly evolving field of density functional theory (DFT), especially the construction of *meta*-generalized gradient approximations (meta-GGAs) has received great attention over the last two decades.[1–4] Modern meta-GGAs use the iso-orbital constraint and the von-Weizäcker inequality to identify one-electron regions and, thus cancelling self-interaction errors in single electron regions.[3,5] According to benchmark calculations,[4,6–21] meta-GGAs outperform the preceding generalized gradient approximations (GGAs) at roughly the same computational cost. However, external magnetic fields[22–25] or spin–orbit coupling[26–28] necessitate further generalizations for meta-GGAs to meet theoretical constrains, as the current density alters the curvature of the Fermi hole in its second-order Taylor expansion.[29–38] Density functional approximations (DFAs) constructed by taking into account this change in curvature are termed "CDFT" functionals.[22,39] CDFT based approximations are for example necessary for the iso-orbital indicator to remain bounded between 0 and 1.[35,36] In external magnetic fields, this correction is even necessary to guarantee gauge-invariance.[22,25,36]

Furthermore, certain current-carrying ground states also heavily depend on the correct introduction of the current density, with a failure to account for them leading to large deviation for meta-GGAs.[36,40] We recently presented a current-dependent formulation of density functional theory for spin–orbit coupling in the molecular regime.[36] Here, inclusion of the current density leads to notable changes for both closed-shell Kramers-restricted (KR) and open-shell Kramers-unrestricted (KU) calculations.

To account for the change in Fermi hole curvature, the kinetic energy density τ is generalized with the current density $\vec{j}$. In a two-component (2c) non-collinear formalism,[41–51] this

results in the generalized current density

$$\tilde{\tau}_{\uparrow,\downarrow} = \tau_{\uparrow,\downarrow} - \frac{|\vec{j}_{\uparrow,\downarrow}|^2}{2n_{\uparrow,\downarrow}} \tag{1}$$

based on the spin-up and down quantities.[36] These are formed with the particle and spin-magnetization contributions, e.g. the spin-up and down electron density $n_{\uparrow,\downarrow}$ follows as

$$n_{\uparrow,\downarrow}(\vec{r}) = \frac{1}{2}\left[n(\vec{r}) \pm |\vec{m}(\vec{r})|\right] = \frac{1}{2}[n(\vec{r}) \pm s(\vec{r})] \tag{2}$$

with the particle density n, the spin-magnetization vector $\vec{m}$, and the spin density s. Therefore, the exchange-correlation (XC) energy of a "pure" functional[2] explicitly depends on the current density

$$\begin{aligned} E^{\mathrm{XC}} &= \int f^{\mathrm{XC}}\left[n_{\uparrow,\downarrow}(\vec{r}), \gamma_{\uparrow\uparrow,\uparrow\downarrow,\downarrow\downarrow}(\vec{r}), \tau_{\uparrow,\downarrow}(\vec{r}), \vec{j}_{\uparrow,\downarrow}(\vec{r})\right]\,\mathrm{d}^3 r \\ &= \int g^{\mathrm{XC}}\left[n_{\uparrow,\downarrow}(\vec{r}), \gamma_{\uparrow\uparrow,\uparrow\downarrow,\downarrow\downarrow}(\vec{r}), \tilde{\tau}_{\uparrow,\downarrow}(\vec{r})\right]\,\mathrm{d}^3 r \end{aligned} \tag{3}$$

where f^{XC} describes the density functional approximation and $\gamma_{\uparrow\downarrow}(\vec{r}) = \frac{1}{4}\left(\vec{\nabla}n_{\uparrow}(\vec{r})\right) \cdot \left(\vec{\nabla}n_{\downarrow}(\vec{r})\right)$, hence $\gamma_{\uparrow\downarrow} = \gamma_{\downarrow\uparrow}$. For a Kramers-restricted system, the spin-magnetization vector and the particle current density vanish. However, the spin-current density is generally non-zero and thus it is still necessary to form the generalized kinetic energy density.

In this work, we will extend our previous CDFT formulation[36] to non-magnetic and magnetic periodic systems. We assess the importance of the current density for band gaps, cell structures, magnetic transitions, and Rashba splittings with common meta-GGAs. Together with previous studies on the impact of spin–orbit-induced current densities for meta-GGAs[36,38,52–54] this will further help to set guidelines and recommendations for the application of CDFT to the different properties and functionals for discrete and periodic systems.

II. THEORY

The one-particle density matrix associated with the two-component spinor functions $\vec{\psi}_i^{\vec{k}}$ at a given $\vec{k}$ point reads

$$n(\vec{r},\vec{r}') = \frac{1}{V_{\text{FBZ}}} \sum_{i=1}^{n} \int_{\text{FBZ}}^{\varepsilon_i^{\vec{k}} < \varepsilon_{\text{F}}} \vec{\psi}_i^{\vec{k}}(\vec{r}) \left(\vec{\psi}_i^{\vec{k}}(\vec{r}') \right)^{\dagger} \mathrm{d}^3 k$$

$$= \begin{pmatrix} n^{\alpha\alpha}(\vec{r},\vec{r}') & n^{\alpha\beta}(\vec{r},\vec{r}') \\ n^{\beta\alpha}(\vec{r},\vec{r}') & n^{\beta\beta}(\vec{r},\vec{r}') \end{pmatrix} \quad (4)$$

where V_{FBZ} is the volume of the first Brillouin zone (FBZ), ε_i the energy eigenvalue, and ε_{F} the Fermi level. The spinor functions are expanded with Bloch functions, ϕ_μ, based on atomic orbital (AO) basis functions, χ_μ, as

$$\vec{\psi}_i^{\vec{k}}(\vec{r}) = \begin{pmatrix} \psi_i^{\alpha,\vec{k}}(\vec{r}) \\ \psi_i^{\beta,\vec{k}}(\vec{r}) \end{pmatrix} = \sum_{\mu} \begin{pmatrix} c_{\mu i}^{\alpha,\vec{k}} \\ c_{\mu i}^{\beta,\vec{k}} \end{pmatrix} \phi_\mu^{\vec{k}}(\vec{r}) \quad (5)$$

$$\phi_\mu^{\vec{k}}(\vec{r}) = \frac{1}{\sqrt{N_{\text{UC}}}} \sum_{\vec{L}} e^{i\vec{k}\cdot\vec{L}} \chi_\mu^{\vec{L}}(\vec{r}). \quad (6)$$

N_{UC} denotes the number of electrons in the unit cell (UC) and $\vec{L}$ the lattice vector. Thus, all density variables are available from the AO density matrix in position space given by

$$D_{\mu\nu}^{\sigma\sigma',\vec{L}\vec{L}'} = \frac{1}{V_{\text{FBZ}}} \sum_i \int_{\text{FBZ}}^{\varepsilon_i^{\vec{k}} < \varepsilon_{\text{F}}} e^{i\vec{k}\cdot[\vec{L}-\vec{L}']} \left(c_{\mu i}^{\sigma,\vec{k}} c_{\nu i}^{*\sigma',\vec{k}} \right) \mathrm{d}^3 k \quad (7)$$

with the expansion coefficients $c_{\mu i}$ and $\sigma, \sigma' \in \{\alpha, \beta\}$. The complete two-component AO density matrix reads

$$\mathbf{D}^{\vec{L}\vec{L}'} = \begin{pmatrix} \mathbf{D}^{\alpha\alpha} & \mathbf{D}^{\alpha\beta} \\ \mathbf{D}^{\beta\alpha} & \mathbf{D}^{\beta\beta} \end{pmatrix}^{\vec{L}\vec{L}'} \quad \text{with} \quad \left(\mathbf{D}^{\vec{L}\vec{L}'} \right)^{\dagger} = \mathbf{D}^{\vec{L}'\vec{L}}. \quad (8)$$

In the spirit of Bulik *et al.*,[47] the real symmetric (RS), real antisymmetric (RA), imaginary symmetric (IS), and imaginary antisymmetric (OA) linear combinations

$$\left[\mathbf{D}_{\text{RS, RA}}^{\sigma\sigma'} \right]^{\vec{L}\vec{L}'} = \frac{1}{2} \left[\text{Re} \left(\mathbf{D}^{\sigma\sigma'} \pm \mathbf{D}^{\sigma'\sigma} \right) \right]^{\vec{L}\vec{L}'} \quad (9)$$

$$\left[\mathbf{D}_{\text{IA, IS}}^{\sigma\sigma'} \right]^{\vec{L}\vec{L}'} = \frac{1}{2} \left[\text{Im} \left(\mathbf{D}^{\sigma\sigma'} \pm \mathbf{D}^{\sigma'\sigma} \right) \right]^{\vec{L}\vec{L}'} \quad (10)$$

are formed. Of course, the same-spin antisymmetric contributions are zero. The electron density and its derivatives are available from the symmetric linear combinations

$$n(\vec{r}) = \sum_{\mu\nu} \sum_{\vec{L}\vec{L}'} \left[\mathbf{D}_{\text{RS}}^{\alpha\alpha} + \mathbf{D}_{\text{RS}}^{\beta\beta} \right]_{\mu\nu}^{\vec{L}\vec{L}'} \chi_\mu^{\vec{L}}(\vec{r}) \chi_\nu^{\vec{L}'}(\vec{r}) \quad (11)$$

$$m_x(\vec{r}) = \sum_{\mu\nu} \sum_{\vec{L}\vec{L}'} 2 \left[\mathbf{D}_{\text{RS}}^{\alpha\beta} \right]_{\mu\nu}^{\vec{L}\vec{L}'} \chi_\mu^{\vec{L}}(\vec{r}) \chi_\nu^{\vec{L}'}(\vec{r}) \quad (12)$$

$$m_y(\vec{r}) = \sum_{\mu\nu} \sum_{\vec{L}\vec{L}'} 2 \left[\mathbf{D}_{\text{IS}}^{\alpha\beta} \right]_{\mu\nu}^{\vec{L}\vec{L}'} \chi_\mu^{\vec{L}}(\vec{r}) \chi_\nu^{\vec{L}'}(\vec{r}) \quad (13)$$

$$m_z(\vec{r}) = \sum_{\mu\nu} \sum_{\vec{L}\vec{L}'} \left[\mathbf{D}_{\text{RS}}^{\alpha\alpha} - \mathbf{D}_{\text{RS}}^{\beta\beta} \right]_{\mu\nu}^{\vec{L}\vec{L}'} \chi_\mu^{\vec{L}}(\vec{r}) \chi_\nu^{\vec{L}'}(\vec{r}). \quad (14)$$

The particle current density $\vec{j}_{\text{p}}$ and the spin-current densities $\vec{j}_u$, with $u \in \{x, y, z\}$, are obtained from the antisymmetric linear combinations

$$\vec{j}_{\text{p}}(\vec{r}) = -\frac{i}{2} \sum_{\mu\nu} \sum_{\vec{L}\vec{L}'} \left[\mathbf{D}_{\text{IA}}^{\alpha\alpha} + \mathbf{D}_{\text{IA}}^{\beta\beta} \right]_{\mu\nu}^{\vec{L}\vec{L}'} \xi_{\mu\nu}^{\vec{L}\vec{L}'} \quad (15)$$

$$\vec{j}_x(\vec{r}) = -\frac{i}{2} \sum_{\mu\nu} \sum_{\vec{L}\vec{L}'} 2 \left[\mathbf{D}_{\text{IA}}^{\alpha\beta} \right]_{\mu\nu}^{\vec{L}\vec{L}'} \xi_{\mu\nu}^{\vec{L}\vec{L}'} \quad (16)$$

$$\vec{j}_y(\vec{r}) = -\frac{i}{2} \sum_{\mu\nu} \sum_{\vec{L}\vec{L}'} 2 \left[\mathbf{D}_{\text{RA}}^{\alpha\beta} \right]_{\mu\nu}^{\vec{L}\vec{L}'} \xi_{\mu\nu}^{\vec{L}\vec{L}'} \quad (17)$$

$$\vec{j}_z(\vec{r}) = -\frac{i}{2} \sum_{\mu\nu} \sum_{\vec{L}\vec{L}'} \left[\mathbf{D}_{\text{IA}}^{\alpha\alpha} - \mathbf{D}_{\text{IA}}^{\beta\beta} \right]_{\mu\nu}^{\vec{L}\vec{L}'} \xi_{\mu\nu}^{\vec{L}\vec{L}'} \quad (18)$$

with

$$\xi_{\mu\nu}^{\vec{L}\vec{L}'} = \left\{ \left[\vec{\nabla}\chi_\mu^{\vec{L}}(\vec{r}) \right] \chi_\nu^{\vec{L}'}(\vec{r}) - \chi_\mu^{\vec{L}}(\vec{r}) \left[\vec{\nabla}\chi_\nu^{\vec{L}'}(\vec{r}) \right] \right\}. \quad (19)$$

Following our molecular ansatz,[36] the scalar part of the XC potential is obtained as

$$V_{\mu\nu,0}^{\text{XC},\vec{L}\vec{L}'} = \frac{1}{2} \int \left[\frac{\partial g^{\text{XC}}}{\partial n_\uparrow} + \frac{\partial g^{\text{XC}}}{\partial n_\downarrow} \right] \chi_\mu^{\vec{L}}(\vec{r}) \chi_\nu^{\vec{L}'}(\vec{r}) \, \mathrm{d}^3 r$$

$$+ \frac{1}{2} \int \left[\frac{|\vec{j}_\uparrow|^2}{2n_\uparrow^2} \frac{\partial g^{\text{XC}}}{\partial n_\downarrow} + \frac{|\vec{j}_\downarrow|^2}{2n_\downarrow^2} \frac{\partial g^{\text{XC}}}{\partial \tilde{\tau}_\downarrow} \right] \chi_\mu^{\vec{L}}(\vec{r}) \chi_\nu^{\vec{L}'}(\vec{r}) \, \mathrm{d}^3 r$$

$$- \frac{1}{2} \int \left[2 \frac{\partial g^{\text{XC}}}{\partial \gamma_{\uparrow\uparrow}} \vec{\nabla}n_\uparrow + 2 \frac{\partial g^{\text{XC}}}{\partial \gamma_{\downarrow\downarrow}} \vec{\nabla}n_\downarrow + \frac{\partial g^{\text{XC}}}{\partial \gamma_{\uparrow\downarrow}} (\vec{\nabla}n_\uparrow + \vec{\nabla}n_\downarrow) \right]$$

$$\left[\left\{ \vec{\nabla}\chi_\mu^{\vec{L}}(\vec{r}) \right\} \chi_\nu^{\vec{L}'}(\vec{r}) + \chi_\mu^{\vec{L}}(\vec{r}) \left\{ \vec{\nabla}\chi_\nu^{\vec{L}'}(\vec{r}) \right\} \right] \mathrm{d}^3 r$$

$$+ \int \frac{1}{2} \left[\frac{\partial g^{\text{XC}}}{\partial \tilde{\tau}_\uparrow} + \frac{\partial g^{\text{XC}}}{\partial \tilde{\tau}_\downarrow} \right] \left[\vec{\nabla}\chi_\mu^{\vec{L}}(\vec{r}) \right] \cdot \left[\vec{\nabla}\chi_\nu^{\vec{L}'}(\vec{r}) \right] \mathrm{d}^3 r$$

$$+ \int \frac{i}{2} \left[\frac{\vec{j}_\uparrow}{n_\uparrow} \frac{\partial g^{\text{XC}}}{\partial \tilde{\tau}_\uparrow} + \frac{\vec{j}_\downarrow}{n_\downarrow} \frac{\partial g^{\text{XC}}}{\partial \tilde{\tau}_\downarrow} \right] \xi_{\mu\nu}^{\vec{L}\vec{L}'} \mathrm{d}^3 r \quad (20)$$

and the spin-magnetization part with $u \in \{x, y, z\}$ reads

$$V_{\mu\nu,u}^{\text{XC},\vec{L}\vec{L}'} = \frac{m_u}{2s} \int \left[\frac{\partial g^{\text{XC}}}{\partial n_\uparrow} - \frac{\partial g^{\text{XC}}}{\partial n_\downarrow} \right] \chi_\mu^{\vec{L}}(\vec{r}) \chi_\nu^{\vec{L}'}(\vec{r}) \, \mathrm{d}^3 r$$

$$+ \frac{m_u}{2s} \int \left[\frac{|\vec{j}_\uparrow|^2}{2n_\uparrow^2} \frac{\partial g^{\text{XC}}}{\partial n_\downarrow} - \frac{|\vec{j}_\downarrow|^2}{2n_\downarrow^2} \frac{\partial g^{\text{XC}}}{\partial \tilde{\tau}_\downarrow} \right] \chi_\mu^{\vec{L}}(\vec{r}) \chi_\nu^{\vec{L}'}(\vec{r}) \, \mathrm{d}^3 r$$

$$- \frac{m_u}{2s} \int \left[2 \frac{\partial g^{\text{XC}}}{\partial \gamma_{\uparrow\uparrow}} \vec{\nabla}n_\uparrow - 2 \frac{\partial g^{\text{XC}}}{\partial \gamma_{\downarrow\downarrow}} \vec{\nabla}n_\downarrow - \frac{\partial g^{\text{XC}}}{\partial \gamma_{\uparrow\downarrow}} (\vec{\nabla}n_\uparrow - \vec{\nabla}n_\downarrow) \right]$$

$$\left[\left\{ \vec{\nabla}\chi_\mu^{\vec{L}}(\vec{r}) \right\} \chi_\nu^{\vec{L}'}(\vec{r}) + \chi_\mu^{\vec{L}}(\vec{r}) \left\{ \vec{\nabla}\chi_\nu^{\vec{L}'}(\vec{r}) \right\} \right] \mathrm{d}^3 r$$

$$+ \int \frac{m_u}{2s} \left[\frac{\partial g^{\text{XC}}}{\partial \tilde{\tau}_\uparrow} - \frac{\partial g^{\text{XC}}}{\partial \tilde{\tau}_\downarrow} \right] \left[\vec{\nabla}\chi_\mu^{\vec{L}}(\vec{r}) \right] \cdot \left[\vec{\nabla}\chi_\nu^{\vec{L}'}(\vec{r}) \right] \mathrm{d}^3 r$$

$$+ i \int \frac{m_u}{2s} \left[\frac{\vec{j}_\uparrow}{n_\uparrow} \frac{\partial g^{\text{XC}}}{\partial \tilde{\tau}_\uparrow} - \frac{\vec{j}_\downarrow}{n_\downarrow} \frac{\partial g^{\text{XC}}}{\partial \tilde{\tau}_\downarrow} \right] \xi_{\mu\nu}^{\vec{L}\vec{L}'} \mathrm{d}^3 r. \quad (21)$$
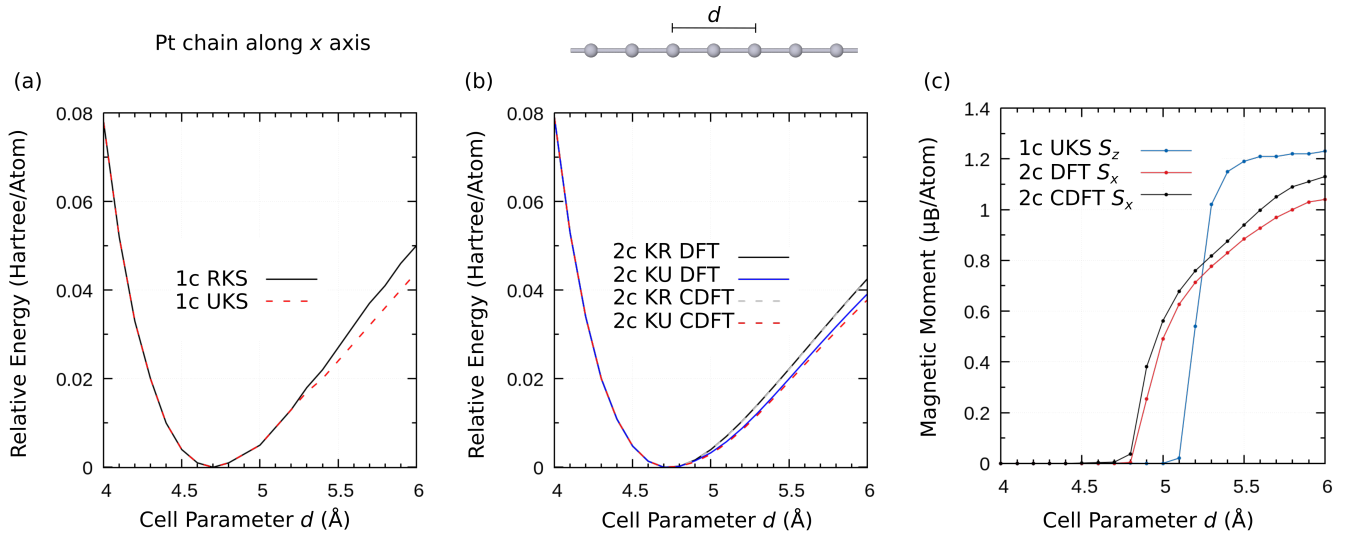
FIG. 1. (a) Dependence of the energy on the cell parameter in units of Hartree per atom for one-component (1c) restricted Kohn–Sham (RKS) and 1c unrestriced Kohn–Sham (UKS) at the TPSS/dhf-SVP-2c level. (b) Dependence of the energy on the cell parameter in units of Hartree per atom for 2c KR and 2c KU with the spin aligned along x (S_x). (c) Magnetic moment in units of Bohr's magneton μ_B per atom for the spin contribution of 1c UKS, 2c KU S_x DFT and CDFT approach. Periodicity is along the x direction for one-dimensional systems.[55] The open-shell solutions are energetically favored compared to the respective closed-shell solutions and the S_x alignment is preferred over $S_{y,z}$. Results without the current-independent TPSS functional are taken from Ref. 56. Detailed results are listed in the Supplementary Material.

The spin blocks of the Kohn–Sham equations are formed by combining the scalar and spin-magnetization contributions with the respective Pauli matrices, c.f. Refs. 36 and 56. After transformation to the k space, the Kohn–Sham equations can be solved as usual.

For non-magnetic or closed-shell system, $\vec{m}$ and $\vec{j}_p$ vanish so that a Kramers-restricted framework can be applied and time-reversal symmetry[57] may be exploited. However, the spin current densities are still non-zero and hence the spin-up and spin-down quantities $\vec{j}_{\uparrow,\downarrow}$ contribute to the XC potential through the diamagnetic or quadratic terms.[36]

The CDFT approach outlined herein is implemented in the riper module[56,58–64] of TURBOMOLE.[65–67] The numerical integration of the exchange-correlation potential is carried with the algorithm of Ref. 59. Note that the current density also leads to antisymmetric contributions. Integration weights are constructed according to Stratmann et al.[68] Geometry gradients and stress tensors are implemented based on previous work, as it essentially involves further derivatives of the basis functions.[56,61,63] We note that all integrals and the exchange potential for the Kohn–Sham equations are evaluated in the position space, which allows to exploit sparsity. The increase in the computational cost by calculating the current density contributions on a grid is modest—especially compared to the inclusion of the current density through Hartree–Fock exchange with hybrid functions.

III. COMPUTATIONAL METHODS

First, we study the impact of the current density on the magnetic transition of one-dimensional linear Pt chains.[69–73] Two

Pt atoms are placed in the unit cell with the cell parameter d ranging from 4.0 Å to 6.0 Å. Calculations are performed at the TPSS/dhf-SVP-2c[74,75] level employing Dirac–Fock effective core potentials (DF-ECPs),[76] replacing 60 electrons (ECP-60). A Gaussian smearing of 0.01 Hartree[77] is used and a k-mesh with 32 points is applied. Integration grids, convergence settings, etc. are given in the Supplementary Material. We note in passing that the Karlsruhe dhf-type basis sets were optimized for discrete systems,[75] however, the corresponding pob-type basis sets for periodic calculations[78–83] are not yet available with tailored extensions for spin–orbit two-component calculations.[84] Therefore and for consistency with previous studies, we apply the dhf-type basis sets.

Second, the band gaps and the Rashba splitting of the transition-metal dichalcogenide monolayers $MoCh_2$ and WCh_2 (Ch = S, Se, Te) in the hexagonal (2H) phase are studied with the M06-L,[85] r^2SCAN,[86,87] TASK,[88] TPSS,[74] Tao–Mo,[5] and PKZB[89] functionals. The GGA PBE[90] serves as reference. The dhf-TZVP-2c basis set[75] is applied with DF-ECPs for Mo (ECP-28), W (ECP-60), Se (ECP-10), Te (ECP-28).[76,91,92] Structures are taken from Ref. 93. A k-mesh of 33×33 points is applied.

Third, the CDFT framework is applied to complement our previous meta-GGA study on silver halides.[56] Here, we consider the TPSS,[74] revTPSS,[94,95] Tao–Mo,[5] PKZB,[89] r^2SCAN,[86,87] and M06-L.[85] We use the dhf-SVP basis set[75] and DF-ECPs are applied for Ag (ECP-28) and I (ECP-28).[96,97] A k-mesh of $7 \times 7 \times 7$ is employed.

IV.   RESULTS AND DISCUSSION

A.   Linear Pt Chain

The one-dimensional linear Pt chain is a common reference system for a transition to a magnetic system. The closed-shell configuration constitutes the electronic ground state with a small cell parameter, whereas the magnetic open-shell solution becomes lower in energy with increasing cell size.[69–73] This is also confirmed at the scalar and spin–orbit TPSS level in Fig. 1. For small cell parameters from $d = 4.0$ to $d = 4.9$ Å, the open-shell initial guess converges to a closed-shell non-magnetic solution in the self-consistent field (SCF) procedure. The most favorable total energy is found for $d = 4.7$ Å in agreement with previous studies based on GGA functionals.[56,72] Further, CDFT and DFT lead to a very similar potential energy surface or a similar behavior of the relative energy with respect to the cell parameter d.

At the scalar level, the transition to a magnetic material occurs between $d \approx 5.2$ Å and $d \approx 5.3$ Å. Inclusion of spin–orbit coupling shifts this transition to a smaller d parameter of about 5.0 Å. Here, the current-dependent variant of TPSS (cTPSS) leads to a lower total energy for both closed-shell and open-shell solutions, i.e. a more negative energy, and a larger magnetic moment. The impact of the current density is generally larger for the magnetic solution than for the closed-shell state, see also the Supplementary Material for detailed results. For the closed-shell solution, the difference in the total energy by inclusion of the current density is too small to be visible in panel (b) of Fig. 1. This finding is qualitatively in line with our previous studies on molecular systems.[36]

Inclusion of the current density also consistently leads to a larger magnetic moment. For instance, TPSS predicts a magnetic moment of $1.04\,\mu_B$/atom at $d = 6.0$ Å, whereas a value of $1.13\,\mu_B$/atom is found with cTPSS. Generally, an increase in the range of 5–8 % is observed after the transition to a magnetic solution.

B.   Transition-Metal Dichalcogenide Monolayers

Transition-metal dichalcogenide monolayers have many interesting physical properties such as the quantum spin Hall,[98] non-linear anomalous Hall,[99] and Rashba effects.[100] In the H2 phase, time-reversal symmetry holds for the non-magnetic systems but space-inversion symmetry is lost. Thus, spin–orbit coupling lifts the degeneracy of the valence band at the K point in the Brillouin zone. For the Mo and W systems, this Rashba splitting is very pronounced and values between 0.1 and 0.5 eV are obtained with relativistic all-electron methods.[93,101]

Band gaps and Rashba splittings at the K point obtained with DFT and CDFT approaches are listed in Tab. I. One the one hand, the impact on the band gaps is rather small, with TASK and r^{2}SCAN showing the largest changes but not exceeding 0.1 eV. Here, the deviation between the different DFAs is far larger. One the other hand, the Rashba splitting is very sensitive to the inclusion of the current density. For

TABLE I. Band gaps and Rashba splittings of the valence band at the K point for transition-metal dichalcogenide monolayers at the 1c DFT, 2c DFT, and 2c CDFT level with the dhf-TZVP-2c basis set and DF-ECPs for all atoms. All values in eV. Results for MoS$_2$ and WS$_2$ are listed in the Supplementary Material.

System	DFA	Band Gap			Rashba Splitting	
		1c DFT	2c DFT	2c CDFT	2c DFT	2c CDFT
MoSe$_2$	PBE	1.554	1.453	–	0.166	–
	PKZB	1.558	1.455	1.455	0.166	0.169
	Tao–Mo	1.561	1.459	1.458	0.166	0.170
	TPSS	1.563	1.459	1.458	0.167	0.174
	M06-L	1.563	1.460	1.455	0.170	0.181
	r^{2}SCAN	1.657	1.554	1.544	0.166	0.189
	TASK	1.735	1.629	1.607	0.172	0.218
MoTe$_2$	PBE	1.157	1.039	–	0.185	–
	PKZB	1.160	1.042	1.042	0.186	0.189
	Tao–Mo	1.168	1.051	1.049	0.185	0.188
	TPSS	1.170	1.051	1.048	0.185	0.195
	M06-L	1.182	1.060	1.053	0.192	0.209
	r^{2}SCAN	1.235	1.116	1.101	0.186	0.218
	TASK	1.287	1.161	1.126	0.197	0.269
WSe$_2$	PBE	1.627	1.324	–	0.409	–
	PKZB	1.652	1.377	1.374	0.407	0.410
	Tao–Mo	1.667	1.371	1.367	0.403	0.411
	TPSS	1.660	1.379	1.371	0.409	0.420
	M06-L	1.668	1.413	1.405	0.422	0.440
	r^{2}SCAN	1.774	1.482	1.452	0.419	0.457
	TASK	1.867	1.604	1.571	0.440	0.514
WTe$_2$	PBE	1.219	0.933	–	0.423	–
	PKZB	1.227	0.953	0.951	0.423	0.427
	Tao–Mo	1.241	0.963	0.957	0.419	0.426
	TPSS	1.237	0.960	0.954	0.422	0.435
	M06-L	1.253	0.968	0.957	0.431	0.456
	r^{2}SCAN	1.325	1.039	1.005	0.436	0.483
	TASK	1.388	1.096	1.050	0.465	0.566

instance, the results change from 0.436 eV to 0.483 eV and 0.465 eV to 0.566 eV for WTe$_2$ with r^{2}SCAN and TASK, respectively.

The most pronounced current-density effects are found for TASK throughout all systems, which is in line with molecular studies.[36,53,102] Here, the current density increase the Rashba splitting by 25 % on average. r^{2}SCAN ranks second in this regard with 13 % followed by M06-L with 6 %. For PKZB, Tao–Mo and TPSS, changes of only 1–3 % are observed. Among the different monolayers, MoTe$_2$ leads to the largest impact of the current density for all DFAs, with a relative deviation of 36 % between DFT and CDFT for TASK. The impact of the current density for the DFAs can be rationalized by the enhancement factor.[102,103]

C.   Silver Halide Crystals

The band gaps and optimized lattice constant of AgI with various meta-GGAs are listed in Tab. II. Results for AgCl and AgBr are presented in the Supplementary Material. Overall, the current density is of minor importance for the band gaps.

TABLE II. Optimized lattice constant a (in Å, rocksalt structure) of three-dimensional AgI and band gaps (in eV) at high symmetry points of the first Brillouin zone with various density functional approximations and the dhf-SVP basis sets. A "c" indicates the current-dependent variant of the DFA. Results for DFAs without inclusion of the current density are taken from Ref. 56, except for M06-L. Calculations are performed without dispersion correction (no D3) and with the D3 correction using Becke–Johnson damping (D3-BJ).

DFA	Dispersion	a	L–L	Γ–Γ	X–X	L–X
TPSS	no D3	6.153	3.249	2.047	2.937	0.583
cTPSS	no D3	6.150	3.244	2.052	2.940	0.579
revTPSS	no D3	6.116	3.149	2.132	2.998	0.537
crevTPSS	no D3	6.098	3.122	2.161	3.014	0.512
Tao–Mo	no D3	6.071	3.099	2.343	3.108	0.616
cTao–Mo	no D3	6.069	3.086	2.339	3.109	0.619
PKZB	no D3	6.200	3.409	2.153	2.987	0.826
cPKZB	no D3	6.210	3.422	2.138	2.979	0.839
r^2SCAN	no D3	6.159	3.776	2.501	3.237	0.911
cr^2SCAN	no D3	6.156	3.772	2.504	3.240	0.907
M06-L	no D3	6.325	3.511	1.891	2.976	1.116
cM06-L	no D3	6.327	3.512	1.889	2.974	1.117
TPSS	D3-BJ	5.982	2.988	2.352	3.098	0.343
cTPSS	D3-BJ	5.980	2.985	2.354	3.099	0.341
revTPSS	D3-BJ	5.949	2.883	2.443	3.156	0.291
crevTPSS	D3-BJ	5.952	2.889	2.435	3.152	0.296
Tao–Mo	D3-BJ	6.068	3.095	2.347	3.110	0.613
cTao–Mo	D3-BJ	6.062	3.087	2.358	3.116	0.604
r^2SCAN	D3-BJ	6.156	3.773	2.506	3.240	0.907
cr^2SCAN	D3-BJ	6.155	3.771	2.506	3.241	0.905

Changes are in the order of meV. These results are in qualitative agreement with the two-dimensional MoTe$_2$ monolayer, which consists of atoms from the same row of the periodic table of elements.

Likewise the current density does not lead to major changes for the cell structure and the lattice constant. The small impact on the lattice constant can be rationalized by the comparably small impact of spin–orbit coupling on the cell structure.[56] D3 dispersion correction with Becke–Johnson damping[8,104–107] (D3-BJ) leads to much larger changes than the application of CDFT. Therefore, other computational parameters than the inclusion of the current density for meta-GGAs are more important for the cell structures of the silver halide crystals.

V. CONCLUSION

We have extended our previous formulation of spin–orbit current density functional theory to periodic systems of arbitrary dimension. The impact of the current density was assessed for various properties of non-magnetic and magnetic systems. Here, the band gaps and lattice constants are not notably affected. In contrast, the Rashba splitting which is only due to spin–orbit coupling is substantially affected. The inclusion of the current density for a given functional may lead to larger changes than the deviation of the results among different functionals.

With the present work, CDFT is now applicable to a wide range of chemical and physical properties of discrete and periodic systems, including analytic first-order property calculations. We generally recommend to include the current density for r^2SCAN and the Minnesota functionals, if available in the used electronic structure code. For TASK, inclusion of the current density is clearly mandatory as it leads to substantial changes of the results.

SUPPLEMENTARY MATERIAL

Supporting Information is available with all computational details and data.

ACKNOWLEDGMENTS

AUTHOR DECLARATIONS

Conflict of Interest

The authors have no conflicts to disclose.

Author Contributions

Yannick J. Franzke: Conceptualization (equal); Data curation (lead); Formal analysis (lead); Investigation (equal); Methodology (lead); Software (lead); Validation (equal); Visualization (lead); Writing – original draft (lead); Writing – review & editing (equal).
Christof Holzer: Conceptualization (equal); Data curation (supporting); Formal analysis (supporting); Investigation (equal); Methodology (supporting); Software (supporting); Validation (equal); Writing – original draft (supporting); Writing – review & editing (equal).

DATA AVAILABILITY STATEMENT

The data that support the findings of this study are available within the article and its supplementary material.

REFERENCES

[1]K. Burke, J. Chem. Phys. **136**, 150901 (2012).
[2]A. D. Becke, J. Chem. Phys. **140**, 18A301 (2014).

[3] J. Sun, A. Ruzsinszky, and J. P. Perdew, Phys. Rev. Lett. **115**, 036402 (2015).

[4] N. Mardirossian and M. Head-Gordon, Mol. Phys. **115**, 2315 (2017).

[5] J. Tao and Y. Mo, Phys. Rev. Lett. **117**, 073001 (2016).

[6] P. Hao, J. Sun, B. Xiao, A. Ruzsinszky, G. I. Csonka, J. Tao, S. Glindmeyer, and J. P. Perdew, J. Chem. Theory Comput. **9**, 355 (2013).

[7] Y. Mo, R. Car, V. N. Staroverov, G. E. Scuseria, and J. Tao, Phys. Rev. B **95**, 035118 (2017).

[8] L. Goerigk, A. Hansen, C. Bauer, S. Ehrlich, A. Najibi, and S. Grimme, Phys. Chem. Chem. Phys. **19**, 32184 (2017).

[9] Y. J. Franzke and J. M. Yu, J. Chem. Theory Comput. **18**, 323 (2022).

[10] Y. J. Franzke and J. M. Yu, J. Chem. Theory Comput. **18**, 2246 (2022).

[11] A. D. Becke, J. Chem. Phys. **156**, 214101 (2022).

[12] P. Borlido, T. Aull, A. W. Huran, F. Tran, M. A. L. Marques, and S. Botti, J. Chem. Theory Comput. **15**, 5069 (2019).

[13] C. Holzer, Y. J. Franzke, and M. Kehry, J. Chem. Theory Comput. **17**, 2928 (2021).

[14] C. Holzer and Y. J. Franzke, J. Chem. Phys. **157**, 034108 (2022).

[15] J. Lee, X. Feng, L. A. Cunha, J. F. Gonthier, E. Epifanovsky, and M. Head-Gordon, J. Chem. Phys. **155**, 164102 (2021).

[16] A. Ghosh, S. Jana, T. Rauch, F. Tran, M. A. L. Marques, S. Botti, L. A. Constantin, M. K. Niranjan, and P. Samal, J. Chem. Phys. **157**, 124108 (2022).

[17] P. Kovás, F. Tran, P. Blaha, and G. K. H. Madsen, J. Chem. Phys. **157**, 094110 (2022).

[18] J. Liang, X. Feng, D. Hait, and M. Head-Gordon, J. Chem. Theory Comput. **18**, 3460 (2022).

[19] Y. J. Franzke, J. Chem. Theory Comput. **19**, 2010 (2023).

[20] P. Kovács, P. Blaha, and G. K. H. Madsen, J. Chem. Phys. **159**, 244118 (2023).

[21] T. Lebeda, T. Aschebrock, J. Sun, L. Leppert, and S. Kümmel, Phys. Rev. Mater. **7**, 093803 (2023).

[22] J. W. Furness, J. Verbeke, E. I. Tellgren, S. Stopkowicz, U. Ekström, T. Helgaker, and A. M. Teale, J. Chem. Theory Comput. **11**, 4169 (2015).

[23] E. I. Tellgren, A. M. Teale, J. W. Furness, K. K. Lange, U. Ekström, and T. Helgaker, J. Chem. Phys. **140**, 034101 (2014).

[24] T. J. P. Irons, G. David, and A. M. Teale, J. Chem. Theory Comput. **17**, 2166 (2021).

[25] A. Pausch and C. Holzer, J. Phys. Chem. Lett. **13**, 4335 (2022).

[26] T. Saue, "Spin-interactions and the non-relativistic limit of electrodynamics," in *Advances in Quantum Chemistry*, Vol. 48, edited by J. R. Sabin, E. Brändas, and L. B. Oddershede (Elsevier Academic Press, San Diego, CA, USA, 2005) pp. 383–405.

[27] T. Saue, ChemPhysChem **12**, 3077 (2011).

[28] P. Pyykkö, Annu. Rev. Phys. Chem. **63**, 45 (2012).

[29] J. F. Dobson, J. Chem. Phys. **98**, 8870 (1993).

[30] J. Tao, Phys. Rev. B **71**, 205107 (2005).

[31] S. Pittalis, S. Kurth, S. Sharma, and E. K. U. Gross, J. Chem. Phys. **127**, 124103 (2007).

[32] E. Räsänen, S. Pittalis, and C. R. Proetto, J. Chem. Phys. **132**, 044112 (2010).

[33] S. Pittalis, E. Räsänen, and E. K. U. Gross, Phys. Rev. A **80**, 032515 (2009).

[34] J. E. Bates and F. Furche, J. Chem. Phys. **137**, 164105 (2012).

[35] T. M. Maier, Y. Ikabata, and H. Nakai, J. Chem. Phys. **152**, 214103 (2020).

[36] C. Holzer, Y. J. Franzke, and A. Pausch, J. Chem. Phys. **157**, 204102 (2022).

[37] J. K. Desmarais, G. Ambrogio, G. Vignale, A. Erba, and S. Pittalis, Phys. Rev. Mater. **8**, 013802 (2024).

[38] J. K. Desmarais, J. Maul, B. Civalleri, A. Erba, G. Vignale, and S. Pittalis, arXiv (2024), 10.48550/arXiv.2401.07581.

[39] E. I. Tellgren, S. Kvaal, E. Sagvolden, U. Ekström, A. M. Teale, and T. Helgaker, Phys. Rev. A **86**, 062506 (2012).

[40] A. D. Becke, J. Chem. Phys. **117**, 6935 (2002).

[41] J. Kübler, K.-H. Höck, J. Sticht, and A. R. Williams, J. Phys. F Metal Phys. **18**, 469 (1988).

[42] C. Van Wüllen, J. Comput. Chem. **23**, 779 (2002).

[43] T. Saue and T. Helgaker, J. Comput. Chem. **23**, 814 (2002).

[44] M. K. Armbruster, F. Weigend, C. van Wüllen, and W. Klopper, Phys. Chem. Chem. Phys. **10**, 1748 (2008).

[45] J. E. Peralta, G. E. Scuseria, and M. J. Frisch, Phys. Rev. B **75**, 125119 (2007).

[46] G. Scalmani and M. J. Frisch, J. Chem. Theory Comput. **8**, 2193 (2012).

[47] I. W. Bulik, G. Scalmani, M. J. Frisch, and G. E. Scuseria, Phys. Rev. B **87**, 035117 (2013).

[48] A. Baldes and F. Weigend, Mol. Phys. **111**, 2617 (2013).

[49] F. Egidi, S. Sun, J. J. Goings, G. Scalmani, M. J. Frisch, and X. Li, J. Chem. Theory Comput. **13**, 2591 (2017).

[50] S. Komorovsky, P. J. Cherry, and M. Repisky, J. Chem. Phys. **151**, 184111 (2019).

[51] J. K. Desmarais, S. Komorovsky, J.-P. Flament, and A. Erba, J. Chem. Phys. **154**, 204110 (2021).

[52] F. Bruder, Y. J. Franzke, and F. Weigend, J. Phys. Chem. A **126**, 5050 (2022).

[53] F. Bruder, Y. J. Franzke, C. Holzer, and F. Weigend, J. Chem. Phys. **159**, 194117 (2023).

[54] Y. J. Franzke, F. Bruder, S. Gillhuber, C. Holzer, and F. Weigend, J. Phys. Chem. A **128**, 670 (2024).

[55] TURBOMOLE GmbH, (2024), manual of TURBOMOLE V7.8.1, a development of University of Karlsruhe and Forschungszentrum Karlsruhe GmbH, 1989-2007, TURBOMOLE GmbH, since 2007; available from https://www.turbomole.org/turbomole/turbomole-documentation/ (retrieved March 4, 2024).

[56] Y. J. Franzke, W. M. Schosser, and F. Pauly, Phys. Rev. B (2024), 10.48550/arXiv.2305.03817, accepted.

[57] J. M. Kasper, A. J. Jenkins, S. Sun, and X. Li, J. Chem. Phys. **153**, 090903 (2020).

[58] A. M. Burow, M. Sierka, and F. Mohamed, J. Chem. Phys. **131**, 214101 (2009).

[59] A. M. Burow and M. Sierka, J. Chem. Theory Comput. **7**, 3097 (2011).

[60] R. Łazarski, A. M. Burow, and M. Sierka, J. Chem. Theory Comput. **11**, 3029 (2015).

[61] R. Łazarski, A. M. Burow, L. Grajciar, and M. Sierka, J. Comput. Chem. **37**, 2518 (2016).

[62] L. Grajciar, J. Comput. Chem. **36**, 1521 (2015).

[63] M. Becker and M. Sierka, J. Comput. Chem. **40**, 2563 (2019).

[64] A. Irmler, A. M. Burow, and F. Pauly, J. Chem. Theory Comput. **14**, 4567 (2018).

[65] R. Ahlrichs, M. Bär, M. Häser, H. Horn, and C. Kölmel, Chem. Phys. Lett. **162**, 165 (1989).

[66] Y. J. Franzke, C. Holzer, J. H. Andersen, T. Begušić, F. Bruder, S. Coriani, F. Della Sala, E. Fabiano, D. A. Fedotov, S. Fürst, S. Gillhuber, R. Grotjahn, M. Kaupp, M. Kehry, M. Krstić, F. Mack, S. Majumdar, B. D. Nguyen, S. M. Parker, F. Pauly, A. Pausch, E. Perlt, G. S. Phun, A. Rajabi, D. Rappoport, B. Samal, T. Schrader, M. Sharma, E. Tapavicza, R. S. Treß, V. Voora, A. Wodyński, J. M. Yu, B. Zerulla, F. Furche, C. Hättig, M. Sierka, D. P. Tew, and F. Weigend, J. Chem. Theory Comput. **19**, 6859 (2023).

[67] TURBOMOLE GmbH, (2024), developers' version of TURBOMOLE V7.8.1, a development of University of Karlsruhe and Forschungszentrum Karlsruhe GmbH, 1989-2007, TURBOMOLE GmbH, since 2007; available from https://www.turbomole.org (retrieved March 4, 2024).

[68] R. Stratmann, G. E. Scuseria, and M. J. Frisch, Chem. Phys. **257**, 213 (1996).

[69] A. Delin and E. Tosatti, Phys. Rev. B **68**, 144434 (2003).

[70] A. Delin and E. Tosatti, Surf. Sci. **566–568**, 262 (2004).

[71] J. Fernández-Rossier, D. Jacob, C. Untiedt, and J. J. Palacios, Phys. Rev. B **72**, 224418 (2005).

[72] A. Smogunov, A. Dal Corso, A. Delin, R. Weht, and E. Tosatti, Nat. Nanotechnol. **3**, 22 (2008).

[73] V. M. García-Suárez, D. Z. Manrique, C. J. Lambert, and J. Ferrer, Phys. Rev. B **79**, 060408(R) (2009).

[74] J. Tao, J. P. Perdew, V. N. Staroverov, and G. E. Scuseria, Phys. Rev. Lett. **91**, 146401 (2003).

[75] F. Weigend and A. Baldes, J. Chem. Phys. **133**, 174102 (2010).

[76] D. Figgen, K. A. Peterson, M. Dolg, and H. Stoll, J. Chem. Phys. **130**, 164108 (2009).

[77] G. Kresse and J. Furthmüller, Comput. Mater. Sci. **6**, 15 (1996).

[78] M. F. Peintinger, D. V. Oliveira, and T. Bredow, J. Comput. Chem. **34**, 451 (2013).

[79] J. Laun, D. Vilela Oliveira, and T. Bredow, J. Comput. Chem. **39**, 1285 (2018).

[80] D. Vilela Oliveira, J. Laun, M. F. Peintinger, and T. Bredow, J. Comput. Chem. **40**, 2364 (2019).

[81] J. Laun and T. Bredow, J. Comput. Chem. **42**, 1064 (2021).

[82] J. Laun and T. Bredow, J. Comput. Chem. **43**, 839 (2022).

[83] L. M. Seidler, J. Laun, and T. Bredow, J. Comput. Chem. **44**, 1418 (2023).

[84] M. K. Armbruster, W. Klopper, and F. Weigend, Phys. Chem. Chem. Phys. **8**, 4862 (2006).

[85] Y. Zhao and D. G. Truhlar, J. Chem. Phys. **125**, 194101 (2006).

[86] J. W. Furness, A. D. Kaplan, J. Ning, J. P. Perdew, and J. Sun, J. Phys. Chem. Lett. **11**, 8208 (2020).

[87] J. W. Furness, A. D. Kaplan, J. Ning, J. P. Perdew, and J. Sun, J. Phys. Chem. Lett. **11**, 9248 (2020).

[88] T. Aschebrock and S. Kümmel, Phys. Rev. Res. **1**, 033082 (2019).

[89] J. P. Perdew, S. Kurth, A. c. v. Zupan, and P. Blaha, Phys. Rev. Lett. **82**, 2544 (1999).

[90] J. P. Perdew, K. Burke, and M. Ernzerhof, Phys. Rev. Lett. **77**, 3865 (1996).

[91] K. A. Peterson, D. Figgen, E. Goll, H. Stoll, and M. Dolg, J. Chem. Phys. **119**, 11113 (2003).

[92] K. A. Peterson, D. Figgen, M. Dolg, and H. Stoll, J. Chem. Phys. **126**, 124101 (2007).

[93] P. Miró, M. Audiffred, and T. Heine, Chem. Soc. Rev. **43**, 6537 (2014).

[94] J. P. Perdew, A. Ruzsinszky, G. I. Csonka, L. A. Constantin, and J. Sun, Phys. Rev. Lett. **103**, 026403 (2009).

[95] J. P. Perdew, A. Ruzsinszky, G. I. Csonka, L. A. Constantin, and J. Sun, Phys. Rev. Lett. **106**, 179902 (2011).

[96] D. Figgen, G. Rauhut, M. Dolg, and H. Stoll, Chem. Phys. **311**, 227 (2005).

[97] K. A. Peterson, B. C. Shepler, D. Figgen, and H. Stoll, J. Phys. Chem. A **110**, 13877 (2006).

[98] C.-C. Liu, W. Feng, and Y. Yao, Phys. Rev. Lett. **107**, 076802 (2011).

[99] K. Kang, T. Li, E. Sohn, J. Shan, and K. F. Mak, Nature Materials **18**, 324 (2019).

[100] Z. Y. Zhu, Y. C. Cheng, and U. Schwingenschlögl, Phys. Rev. B **84**, 153402 (2011).

[101] M. Kadek, B. Wang, M. Joosten, W.-C. Chiu, F. Mairesse, M. Repisky, K. Ruud, and A. Bansil, Phys. Rev. Mater. **7**, 064001 (2023).

[102] Y. J. Franzke and C. Holzer, J. Chem. Phys. **157**, 031102 (2022).

[103] R. Grotjahn, F. Furche, and M. Kaupp, J. Chem. Phys. **157**, 111102 (2022).

[104] S. Grimme, J. Antony, S. Ehrlich, and H. Krieg, J. Chem. Phys. **132**, 154104 (2010).

[105] S. Grimme, S. Ehrlich, and L. Goerigk, J. Comput. Chem. **32**, 1456 (2011).

[106] A. Patra, S. Jana, L. A. Constantin, and P. Samal, J. Chem. Phys. **153**, 084117 (2020).

[107] S. Ehlert, U. Huniar, J. Ning, J. W. Furness, J. Sun, A. D. Kaplan, J. P. Perdew, and J. G. Brandenburg, J. Chem. Phys. **154**, 061101 (2021).

Supplementary Material for "Current density functional framework for spin–orbit coupling: Extension to periodic systems"

Yannick J. Franzke[1] and Christof Holzer[2]

[1]*Otto Schott Institute of Materials Research, Friedrich Schiller University Jena, Löbdergraben 32, 07743 Jena, Germany*

[2]*Institute of Theoretical Solid State Physics, Karlsruhe Institute of Technology (KIT), Wolfgang-Gaede-Straße 1, 76131 Karlsruhe, Germany*

(*Email for correspondence: christof.holzer@kit.edu)

(*Email for correspondence: yannick.franzke@uni-jena.de)

(Dated: 21 March 2024)

CONTENTS

I. LINEAR ONE-DIMENSIONAL PT CHAIN

A. Computational Details and Detailed Results

Two Pt atoms are placed in a unit cell with a cell parameter d. Relativistic effects are introduced through small-core Dirac–Fock effective core potentials (ECP-60).[1] The dhf-SVP-2c orbital and auxiliary basis sets are applied[2] and large integration grids[3,4] (grid size 4) are employed for the numerical integration of the exchange-correlation potential[5] with the TPSS functional.[6] Note that the riper module uses the resolution of the identity approximation (RI-*J*) in combination with the continuous fast multipole method (CFMM).[7,8] Default settings are employed for RI-*J*, CFMM, and the transformation to the orthogonal basis set for the diagonalization of the Kohn–Sham or Fock matrix.[8,9] A Gaussian smearing of 0.01 Hartree is applied[10] and a k-mesh of 32 points is used. The self-consistent field (SCF) procedure is converged with a threshold of 10^{-8} Hartree. Kramers-restricted (KR) and Kramers-unrestricted (KU) calculations are started from a molecular extended Hückel guess with a closed-shell configuration and an open-shell configuration using four unpaired electrons, respectively. For the KU calculations, the initial wavefunction is chosen to be an eigenfunction of the spin operator $\hat{S}_x$. Periodicity is also assumed along the x direction.[9] Structures in TURBOMOLE format[9,11–15] are available from Ref. 16. Results are listed in Tab. I. Here, the CDFT energies are always lower than the DFT energy, i.e. a more negative energy is found.

TABLE I. Total SCF energies in Hartree obtained with the 2c KR DFT, 2c KU DFT, 2c KR CDFT, and 2c KU CDFT approach, and energies for the limit of a vanishing Gaussian smearing (limit). The expectation values of spin S_x are listed for the open-shell calculations. The TPSS functional[6] is employed with the dhf-SVP-2c basis set[2] and a Dirac–Fock ECP for Pt.[1] 2c DFT results are taken from Ref. 16.

d	KR DFT limit	KR DFT	KR CDFT limit	KR CDFT	KU DFT limit	KU DFT	KU DFT $\langle S_x \rangle$	KU CDFT limit	KU CDFT	KU CDFT $\langle S_x \rangle$
4.0	−239.0074	−239.0065	−239.0077	−239.0067	−239.0074	−239.0065	3.62×10^{-5}	−239.0076	−239.0067	2.64×10^{-8}
4.1	−239.0592	−239.0580	−239.0594	−239.0583	−239.0592	−239.0580	2.35×10^{-5}	−239.0594	−239.0583	-1.00×10^{-14}
4.2	−239.0975	−239.0961	−239.0977	−239.0963	−239.0975	−239.0961	4.72×10^{-5}	−239.0977	−239.0963	1.00×10^{-14}
4.3	−239.1251	−239.1234	−239.1254	−239.1237	−239.1251	−239.1234	3.41×10^{-4}	−239.1253	−239.1236	2.08×10^{-4}
4.4	−239.1443	−239.1423	−239.1446	−239.1425	−239.1443	−239.1423	4.77×10^{-4}	−239.1446	−239.1425	7.00×10^{-14}
4.5	−239.1568	−239.1544	−239.1571	−239.1547	−239.1568	−239.1544	5.10×10^{-4}	−239.1570	−239.1546	1.69×10^{-3}
4.6	−239.1641	−239.1613	−239.1644	−239.1616	−239.1641	−239.1613	5.05×10^{-4}	−239.1643	−239.1615	3.40×10^{-3}
4.7	−239.1672	−239.1640	−239.1675	−239.1643	−239.1672	−239.1640	3.94×10^{-4}	−239.1675	−239.1642	5.12×10^{-3}
4.8	−239.1672	−239.1636	−239.1675	−239.1639	−239.1672	−239.1636	3.97×10^{-3}	−239.1675	−239.1638	3.72×10^{-2}
4.9	−239.1648	−239.1607	−239.1651	−239.1610	−239.1650	−239.1611	2.54×10^{-1}	−239.1656	−239.1618	3.81×10^{-1}
5.0	−239.1606	−239.1560	−239.1609	−239.1564	−239.1614	−239.1575	4.91×10^{-1}	−239.1621	−239.1583	5.62×10^{-1}
5.1	−239.1550	−239.1501	−239.1554	−239.1504	−239.1565	−239.1525	6.27×10^{-1}	−239.1573	−239.1534	6.78×10^{-1}
5.2	−239.1486	−239.1432	−239.1489	−239.1436	−239.1506	−239.1464	7.13×10^{-1}	−239.1515	−239.1474	7.59×10^{-1}
5.3	−239.1415	−239.1357	−239.1418	−239.1361	−239.1439	−239.1395	7.76×10^{-1}	−239.1449	−239.1406	8.18×10^{-1}
5.4	−239.1340	−239.1278	−239.1343	−239.1282	−239.1367	−239.1320	8.30×10^{-1}	−239.1379	−239.1332	8.76×10^{-1}
5.5	−239.1262	−239.1197	−239.1266	−239.1201	−239.1293	−239.1241	8.84×10^{-1}	−239.1306	−239.1256	9.39×10^{-1}
5.6	−239.1183	−239.1115	−239.1187	−239.1118	−239.1217	−239.1162	9.27×10^{-1}	−239.1232	−239.1179	9.98×10^{-1}
5.7	−239.1104	−239.1032	−239.1108	−239.1036	−239.1141	−239.1083	9.69×10^{-1}	−239.1159	−239.1104	1.05
5.8	−239.1025	−239.0950	−239.1029	−239.0954	−239.1067	−239.1006	1.00	−239.1087	−239.1030	1.09
5.9	−239.0948	−239.0869	−239.0952	−239.0873	−239.0994	−239.0931	1.03	−239.1017	−239.0958	1.11
6.0	−239.0873	−239.0791	−239.0877	−239.0795	−239.0924	−239.0859	1.04	−239.0948	−239.0887	1.13

II. TWO-DIMENSIONAL TRANSITION-METAL DICHALCOGENIDE MONOLAYERS

A. Computational Details

Band gaps and Rashba splittings are calculated for the transition-metal dichalcogenide monolayers MoS_2, $MoSe_2$, $MoTe_2$, WS_2, WSe_2, and WTe_2 with the PBE,[17] M06-L,[18] r^2SCAN,[19,20] TASK,[21] TPSS,[6] Tao–Mo,[22] and PKZB[23] density functional approximations (DFAs). Note that we use Libxc[24–26] for M06-L, r^2SCAN, TASK, Tao–Mo, and PKZB. The dhf-TZVP-2c orbital and auxiliary basis sets are applied.[2] Originally, the dhf-type basis sets only employ ECPs for elements beyond Kr. That is, Dirac–Fock ECPs are employed for Mo (ECP-28), W (ECP-60), and Te (ECP-28).[1,27,28] However, this leads to rather large deviations from the relativistic all-electron calculations at the PBE level for $MoSe_2$ and WSe_2.[29,30] See Tabs. II and III. Therefore, we applied a small-core Dirac–Fock ECP for Se (ECP-10) as well.[27,31] The corresponding results are shown in Tabs. IV and V.

Large integration grids[3,4] (grid size 3) are employed for the numerical integration of the exchange-correlation potential.[5] Again, default settings are applied for RI-*J*, CFMM, and the transformation to the orthogonal basis set for the diagonalization of the Kohn–Sham or Fock matrix.[8,9] The SCF procedure is converged with a threshold of 10^{-7} Hartree and a *k*-mesh of 33×33 points is used. Structures are taken from Ref. 29.

B. Results

TABLE II. Band gaps and Rashba splittings of the valence band at the K point for transition-metal dichalcogenide monolayers at the 1c DFT, 2c DFT, and 2c CDFT level with the dhf-TZVP-2c basis set and DF-ECPs for Mo and Te. All values in eV.

| System | DFA | Band Gap | | | Rashba Splitting | |
		1c DFT	2c DFT	2c CDFT	2c DFT	2c CDFT
MoS_2	PBE	1.827	1.757	1.755	0.102	0.102
	M06-L	1.814	1.772	1.772	0.107	0.112
	r^2SCAN	1.940	1.884	1.879	0.103	0.116
	TASK	2.035	1.979	1.968	0.105	0.130
	TPSS	1.829	1.775	1.774	0.102	0.106
	Tao–Mo	1.828	1.774	1.773	0.101	0.104
	PKZB	1.829	1.775	1.774	0.101	0.103
$MoSe_2$	PBE	1.560	1.504	1.504	0.102	0.102
	M06-L	1.567	1.509	1.508	0.107	0.113
	r^2SCAN	1.658	1.602	1.596	0.104	0.119
	TASK	1.738	1.681	1.669	0.107	0.135
	TPSS	1.566	1.510	1.508	0.103	0.107
	Tao–Mo	1.564	1.508	1.508	0.102	0.105
	PKZB	1.562	1.506	1.506	0.102	0.104
$MoTe_2$	PBE	1.157	1.039	1.039	0.185	0.185
	M06-L	1.182	1.060	1.053	0.192	0.209
	r^2SCAN	1.235	1.116	1.101	0.186	0.218
	TASK	1.287	1.161	1.126	0.197	0.269
	TPSS	1.170	1.051	1.048	0.185	0.195
	Tao–Mo	1.168	1.051	1.049	0.185	0.188
	PKZB	1.160	1.042	1.042	0.186	0.189

TABLE III. Band gaps and Rashba splittings of the valence band at the K point for transition-metal dichalcogenide monolayers at the 1c DFT, 2c DFT, and 2c CDFT level with the dhf-TZVP-2c basis set and DF-ECPs for W and Te. All values in eV.

System	DFA	Band Gap			Rashba Splitting	
		1c DFT	2c DFT	2c CDFT	2c DFT	2c CDFT
WS_2	PBE	1.999	1.697	1.697	0.343	0.343
	M06-L	2.024	1.803	1.798	0.357	0.369
	r^2SCAN	2.156	1.868	1.845	0.351	0.379
	TASK	2.261	2.037	2.006	0.364	0.416
	TPSS	2.031	1.758	1.752	0.343	0.351
	Tao–Mo	2.040	1.754	1.749	0.337	0.343
	PKZB	2.023	1.752	1.750	0.339	0.342
WSe_2	PBE	1.654	1.385	1.385	0.354	0.354
	M06-L	1.676	1.447	1.440	0.366	0.381
	r^2SCAN	1.782	1.534	1.507	0.363	0.395
	TASK	1.872	1.637	1.610	0.378	0.440
	TPSS	1.672	1.436	1.429	0.353	0.362
	Tao–Mo	1.680	1.433	1.427	0.347	0.354
	PKZB	1.664	1.435	1.433	0.350	0.353
WTe_2	PBE	1.219	0.933	0.933	0.423	0.423
	M06-L	1.253	0.968	0.957	0.431	0.456
	r^2SCAN	1.325	1.039	1.005	0.436	0.483
	TASK	1.388	1.096	1.050	0.465	0.566
	TPSS	1.237	0.960	0.954	0.422	0.435
	Tao–Mo	1.241	0.963	0.957	0.419	0.426
	PKZB	1.227	0.953	0.951	0.423	0.427

TABLE IV. Band gaps and Rashba splittings of the valence band at the K point for transition-metal dichalco-genide monolayers at the 1c DFT, 2c DFT, and 2c CDFT level with the dhf-TZVP-2c basis set and DF-ECPs for Mo, Se, and Te. All values in eV.

		Band Gap			Rashba Splitting	
System	DFA	1c DFT	2c DFT	2c CDFT	2c DFT	2c CDFT
MoS_2	PBE	1.827	1.757	1.755	0.102	0.102
	M06-L	1.814	1.772	1.772	0.107	0.112
	r^2SCAN	1.940	1.884	1.879	0.103	0.116
	TASK	2.035	1.979	1.968	0.105	0.130
	TPSS	1.829	1.775	1.774	0.102	0.106
	Tao–Mo	1.828	1.774	1.773	0.101	0.104
	PKZB	1.829	1.775	1.774	0.101	0.103
$MoSe_2$	PBE	1.554	1.453	–	0.166	–
	PKZB	1.558	1.455	1.455	0.166	0.169
	Tao–Mo	1.561	1.459	1.458	0.166	0.170
	TPSS	1.563	1.459	1.458	0.167	0.174
	M06-L	1.563	1.460	1.455	0.170	0.181
	r^2SCAN	1.657	1.554	1.544	0.166	0.189
	TASK	1.735	1.629	1.607	0.172	0.218
$MoTe_2$	PBE	1.157	1.039	–	0.185	–
	PKZB	1.160	1.042	1.042	0.186	0.189
	Tao–Mo	1.168	1.051	1.049	0.185	0.188
	TPSS	1.170	1.051	1.048	0.185	0.195
	M06-L	1.182	1.060	1.053	0.192	0.209
	r^2SCAN	1.235	1.116	1.101	0.186	0.218
	TASK	1.287	1.161	1.126	0.197	0.269

TABLE V. Band gaps and Rashba splittings of the valence band at the K point for transition-metal dichalcogenide monolayers at the 1c DFT, 2c DFT, and 2c CDFT level with the dhf-TZVP-2c basis set and DF-ECPs for W, Se, and Te. All values in eV.

System	DFA	Band Gap			Rashba Splitting	
		1c DFT	2c DFT	2c CDFT	2c DFT	2c CDFT
WS_2	PBE	1.999	1.697	1.697	0.343	0.343
	M06-L	2.024	1.803	1.798	0.357	0.369
	r^2SCAN	2.156	1.868	1.845	0.351	0.379
	TASK	2.261	2.037	2.006	0.364	0.416
	TPSS	2.031	1.758	1.752	0.343	0.351
	Tao–Mo	2.040	1.754	1.749	0.337	0.343
	PKZB	2.023	1.752	1.750	0.339	0.342
WSe_2	PBE	1.627	1.324	–	0.409	–
	PKZB	1.652	1.377	1.374	0.407	0.410
	Tao–Mo	1.667	1.371	1.367	0.403	0.411
	TPSS	1.660	1.379	1.371	0.409	0.420
	M06-L	1.668	1.413	1.405	0.422	0.440
	r^2SCAN	1.774	1.482	1.452	0.419	0.457
	TASK	1.867	1.604	1.571	0.440	0.514
WTe_2	PBE	1.219	0.933	–	0.423	–
	PKZB	1.227	0.953	0.951	0.423	0.427
	Tao–Mo	1.241	0.963	0.957	0.419	0.426
	TPSS	1.237	0.960	0.954	0.422	0.435
	M06-L	1.253	0.968	0.957	0.431	0.456
	r^2SCAN	1.325	1.039	1.005	0.436	0.483
	TASK	1.388	1.096	1.050	0.465	0.566

III. THREE-DIMENSIONAL SILVER HALIDE CRYSTALS

A. Computational Details

Silver halide systems are commonly studied with relativistic methods[32–34] and we have previously calculated the band gaps and cell structure with various meta-GGAs in DFT framework.[16] Thus, we complement these results with the CDFT treatment. Computational settings are chosen accordingly. That is, the dhf-SVP orbital and auxiliary basis sets[2] are applied with small-core Dirac–Fock ECPs (ECP-28) for Ag and I.[35,36] The TPSS,[6] revTPSS,[37,38] Tao–Mo,[22] PKZB,[23] r^{2}SCAN,[19,20] and M06-L[18] density functional approximations are used with large integration grids (grid size 4).[3,4] We use Libxc[24–26] for revTPSS, Tao–Mo, PKZB and M06-L. The D3 dispersion correction is applied if available for the given DFA.[39–43] Default settings are chosen for RI-J, CFMM, and the transformation to the orthogonal basis set for the diagonalization of the Kohn–Sham or Fock matrix.[8,9] An SCF convergence threshold of 10^{-7} Hartree is applied and a k-mesh of $7 \times 7 \times 7$ point is employed. Cell structures are optimized with weight derivatives and an energy threshold of 10^{-6} Hartree.[44] Results for AgCl, AgBr, and AgI are listed in Tabs. VI, VII, and VIII, respectively. Inclusion of the current density in the exchange-correlation potential is indicated by a "c" for the functional acronym. Initial cell structures were taken from Ref. 16.

B. Results

TABLE VI. Optimized lattice constant a (in Å, rocksalt structure) of three-dimensional AgCl and band gaps (in eV) at high symmetry points of the first Brillouin zone with various density functional approximations and the dhf-SVP basis sets.[2] A Dirac–Fock ECP is applied for Ag (ECP-28).[35] A "c" indicates the current-dependent variant of the DFA. Results for DFAs without inclusion of the current density are taken from Ref. 16, except for M06-L. Calculations are performed without dispersion correction (no D3) and with the D3 correction using Becke–Johnson damping (D3-BJ).[39,40]

DFA	Dispersion	a	L–L	Γ–Γ	X–X	L–Γ
TPSS	no D3	5.586	4.553	3.042	4.135	0.966
cTPSS	no D3	5.578	4.539	3.056	4.138	0.964
revTPSS	no D3	5.561	4.381	3.023	4.126	0.890
crevTPSS	no D3	5.542	4.350	3.059	4.135	0.885
Tao–Mo	no D3	5.541	4.242	3.099	4.238	0.971
cTao-Mo	no D3	5.518	4.212	3.150	4.251	0.971
PKZB	no D3	5.636	4.593	3.099	4.259	1.176
cPKZB	no D3	5.644	4.604	3.086	4.256	1.178
r^2SCAN	no D3	5.576	5.017	3.545	4.564	1.413
cr^2SCAN	no D3	5.564	5.001	3.570	4.569	1.413
M06-L	no D3	5.636	4.947	3.357	4.654	1.464
cM06-L	no D3	5.640	4.951	3.349	4.649	1.464
TPSS	D3-BJ	5.498	4.400	3.213	4.175	0.943
cTPSS	D3-BJ	5.461	4.334	3.293	4.193	0.937
revTPSS	D3-BJ	5.476	4.233	3.204	4.169	0.873
crevTPSS	D3-BJ	5.445	4.179	3.274	4.184	0.870
Tao–Mo	D3-BJ	5.511	4.203	3.166	4.255	0.971
cTao-Mo	D3-BJ	5.499	4.186	3.194	4.262	0.972
r^2SCAN	D3-BJ	5.517	4.943	3.677	4.592	1.416
cr^2SCAN	D3-BJ	5.514	4.939	3.683	4.592	1.416

TABLE VII. Optimized lattice constant a (in Å, rocksalt structure) of three-dimensional AgBr and band gaps (in eV) at high symmetry points of the first Brillouin zone with various density functional approximations and the dhf-SVP basis sets.[2] A Dirac–Fock ECP is applied for Ag (ECP-28).[35] A "c" indicates the current-dependent variant of the DFA. Results for DFAs without inclusion of the current density are taken from Ref. 16, except for M06-L. Calculations are performed without dispersion correction (no D3) and with the D3 correction using Becke–Johnson damping (D3-BJ).[39,40]

DFA	Dispersion	a	L–L	Γ–Γ	X–X	L–Γ
TPSS	no D3	5.812	3.988	2.899	3.677	0.950
cTPSS	no D3	5.802	3.971	2.918	3.679	0.949
revTPSS	no D3	5.784	3.871	2.963	3.667	0.936
crevTPSS	no D3	5.764	3.839	2.999	3.672	0.936
Tao–Mo	no D3	5.738	3.781	3.140	3.792	1.079
cTao-Mo	no D3	5.736	3.779	3.143	3.792	1.079
PKZB	no D3	5.868	4.128	2.985	3.812	1.189
cPKZB	no D3	5.875	4.138	2.973	3.812	1.190
r^2SCAN	no D3	5.811	4.501	3.361	4.094	1.416
cr^2SCAN	no D3	5.800	4.486	3.384	4.095	1.418
M06-L	no D3	5.909	4.440	3.134	4.204	1.452
cM06-L	no D3	5.916	4.447	3.120	4.199	1.450
TPSS	D3-BJ	5.708	3.815	3.092	3.708	0.951
cTPSS	D3-BJ	5.673	3.754	3.163	3.719	0.956
revTPSS	D3-BJ	5.690	3.715	3.143	3.695	0.942
crevTPSS	D3-BJ	5.655	3.653	3.218	3.707	0.948
Tao–Mo	D3-BJ	5.743	3.789	3.128	3.790	1.077
cTao–Mo	D3-BJ	5.731	3.771	3.155	3.794	1.080
r^2SCAN	D3-BJ	5.774	4.448	3.444	4.104	1.423
cr^2SCAN	D3-BJ	5.758	4.429	3.473	4.107	1.426

TABLE VIII. Optimized lattice constant a (in Å, rocksalt structure) of three-dimensional AgI and band gaps (in eV) at high symmetry points of the first Brillouin zone with various density functional approximations and the dhf-SVP basis sets.[2] Dirac–Fock ECPs are applied for Ag (ECP-28) and I (ECP-28).[35,36] A "c" indicates the current-dependent variant of the DFA. Results for DFAs without inclusion of the current density are taken from Ref. 16, except for M06-L. Calculations are performed without dispersion correction (no D3) and with the D3 correction using Becke–Johnson damping (D3-BJ).[39,40]

DFA	Dispersion	a	L–L	Γ–Γ	X–X	L–X
TPSS	no D3	6.153	3.249	2.047	2.937	0.583
cTPSS	no D3	6.150	3.244	2.052	2.940	0.579
revTPSS	no D3	6.116	3.149	2.132	2.998	0.537
crevTPSS	no D3	6.098	3.122	2.161	3.014	0.512
Tao–Mo	no D3	6.071	3.099	2.343	3.108	0.616
cTao–Mo	no D3	6.069	3.086	2.339	3.109	0.619
PKZB	no D3	6.200	3.409	2.153	2.987	0.826
cPKZB	no D3	6.210	3.422	2.138	2.979	0.839
r^2SCAN	no D3	6.159	3.776	2.501	3.237	0.911
cr^{2}SCAN	no D3	6.156	3.772	2.504	3.240	0.907
M06-L	no D3	6.325	3.511	1.891	2.976	1.116
cM06-L	no D3	6.327	3.512	1.889	2.974	1.117
TPSS	D3-BJ	5.982	2.988	2.352	3.098	0.343
cTPSS	D3-BJ	5.980	2.985	2.354	3.099	0.341
revTPSS	D3-BJ	5.949	2.883	2.443	3.156	0.291
crevTPSS	D3-BJ	5.952	2.889	2.435	3.152	0.296
Tao–Mo	D3-BJ	6.068	3.095	2.347	3.110	0.613
cTao–Mo	D3-BJ	6.062	3.087	2.358	3.116	0.604
r^2SCAN	D3-BJ	6.156	3.773	2.506	3.240	0.907
cr^{2}SCAN	D3-BJ	6.155	3.771	2.506	3.241	0.905

REFERENCES

[1] D. Figgen, K. A. Peterson, M. Dolg, and H. Stoll, J. Chem. Phys. **130**, 164108 (2009).

[2] F. Weigend and A. Baldes, J. Chem. Phys. **133**, 174102 (2010).

[3] O. Treutler and R. Ahlrichs, J. Chem. Phys. **102**, 346 (1995).

[4] O. Treutler, *Entwicklung und Anwendung von Dichtefunktionalmethoden*, Dissertation (Dr. rer. nat.), University of Karlsruhe (TH), Germany (1995).

[5] A. M. Burow and M. Sierka, J. Chem. Theory Comput. **7**, 3097 (2011).

[6] J. Tao, J. P. Perdew, V. N. Staroverov, and G. E. Scuseria, Phys. Rev. Lett. **91**, 146401 (2003).

[7] A. M. Burow, M. Sierka, and F. Mohamed, J. Chem. Phys. **131**, 214101 (2009).

[8] R. Łazarski, A. M. Burow, and M. Sierka, J. Chem. Theory Comput. **11**, 3029 (2015).

[9] TURBOMOLE GmbH, (2024), manual of TURBOMOLE V7.8.1, a development of University of Karlsruhe and Forschungszentrum Karlsruhe GmbH, 1989-2007, TURBO-MOLE GmbH, since 2007; available from `https://www.turbomole.org/turbomole/turbomole-documentation/` (retrieved March 4, 2024).

[10] G. Kresse and J. Furthmüller, Comput. Mater. Sci. **6**, 15 (1996).

[11] R. Ahlrichs, M. Bär, M. Häser, H. Horn, and C. Kölmel, Chem. Phys. Lett. **162**, 165 (1989).

[12] F. Furche, R. Ahlrichs, C. Hättig, W. Klopper, M. Sierka, and F. Weigend, Wiley Interdiscip. Rev.: Comput. Mol. Sci. **4**, 91 (2014).

[13] S. G. Balasubramani, G. P. Chen, S. Coriani, M. Diedenhofen, M. S. Frank, Y. J. Franzke, F. Furche, R. Grotjahn, M. E. Harding, C. Hättig, A. Hellweg, B. Helmich-Paris, C. Holzer, U. Huniar, M. Kaupp, A. Marefat Khah, S. Karbalaei Khani, T. Müller, F. Mack, B. D. Nguyen, S. M. Parker, E. Perlt, D. Rappoport, K. Reiter, S. Roy, M. Rückert, G. Schmitz, M. Sierka, E. Tapavicza, D. P. Tew, C. van Wüllen, V. K. Voora, F. Weigend, A. Wodyński, and J. M. Yu, J. Chem. Phys. **152**, 184107 (2020).

[14] Y. J. Franzke, C. Holzer, J. H. Andersen, T. Begušić, F. Bruder, S. Coriani, F. Della Sala, E. Fabiano, D. A. Fedotov, S. Fürst, S. Gillhuber, R. Grotjahn, M. Kaupp, M. Kehry, M. Krstić, F. Mack, S. Majumdar, B. D. Nguyen, S. M. Parker, F. Pauly, A. Pausch, E. Perlt, G. S. Phun, A. Rajabi, D. Rappoport, B. Samal, T. Schrader, M. Sharma, E. Tapavicza, R. S. Treß, V. Voora, A. Wodyński, J. M. Yu, B. Zerulla, F. Furche, C. Hättig, M. Sierka, D. P. Tew, and F. Weigend, J. Chem. Theory Comput. **19**, 6859 (2023).

[15] TURBOMOLE GmbH, (2024), developers' version of TURBOMOLE V7.8.1, a development of University of Karlsruhe and Forschungszentrum Karlsruhe GmbH, 1989-2007, TURBOMOLE GmbH, since 2007; available from `https://www.turbomole.org` (retrieved March 4, 2024).

[16] Y. J. Franzke, W. M. Schosser, and F. Pauly, Phys. Rev. B (2024), 10.48550/arXiv.2305.03817, accepted.

[17] J. P. Perdew, K. Burke, and M. Ernzerhof, Phys. Rev. Lett. **77**, 3865 (1996).

[18] Y. Zhao and D. G. Truhlar, J. Chem. Phys. **125**, 194101 (2006).

[19] J. W. Furness, A. D. Kaplan, J. Ning, J. P. Perdew, and J. Sun, J. Phys. Chem. Lett. **11**, 8208 (2020).

[20] J. W. Furness, A. D. Kaplan, J. Ning, J. P. Perdew, and J. Sun, J. Phys. Chem. Lett. **11**, 9248 (2020).

[21] T. Aschebrock and S. Kümmel, Phys. Rev. Res. **1**, 033082 (2019).

[22] J. Tao and Y. Mo, Phys. Rev. Lett. **117**, 073001 (2016).

[23] J. P. Perdew, S. Kurth, A. c. v. Zupan, and P. Blaha, Phys. Rev. Lett. **82**, 2544 (1999).

[24] M. A. L. Marques, M. J. T. Oliveira, and T. Burnus, Comput. Phys. Commun. **183**, 2272 (2012).

[25] S. Lehtola, C. Steigemann, M. J. T. Oliveira, and M. A. L. Marques, SoftwareX **7**, 1 (2018).

[26] "Libxc," Version 6.2.2, available from `https://www.tddft.org/programs/libxc/` (retrieved July 26, 2023).

[27] K. A. Peterson, D. Figgen, E. Goll, H. Stoll, and M. Dolg, J. Chem. Phys. **119**, 11113 (2003).

[28] K. A. Peterson, D. Figgen, M. Dolg, and H. Stoll, J. Chem. Phys. **126**, 124101 (2007).

[29] P. Miró, M. Audiffred, and T. Heine, Chem. Soc. Rev. **43**, 6537 (2014).

[30] M. Kadek, B. Wang, M. Joosten, W.-C. Chiu, F. Mairesse, M. Repisky, K. Ruud, and A. Bansil, Phys. Rev. Mater. **7**, 064001 (2023).

[31] M. Dolg, Effective core potentials of Se (ECP10MDF) taken from `https://www.tc.uni-koeln.de/PP/clickpse.en.html` (retrieved March 19, 2024).

[32] J. E. Peralta, J. Uddin, and G. E. Scuseria, J. Chem. Phys. **122**, 084108 (2005).

[33] R. Zhao, Y. Zhang, Y. Xiao, and W. Liu, J. Chem. Phys. **144**, 044105 (2016).

[34] M. Kadek, M. Repisky, and K. Ruud, Phys. Rev. B **99**, 205103 (2019).

[35] D. Figgen, G. Rauhut, M. Dolg, and H. Stoll, Chem. Phys. **311**, 227 (2005).

[36] K. A. Peterson, B. C. Shepler, D. Figgen, and H. Stoll, J. Phys. Chem. A **110**, 13877 (2006).

[37] J. P. Perdew, A. Ruzsinszky, G. I. Csonka, L. A. Constantin, and J. Sun, Phys. Rev. Lett. **103**, 026403 (2009).

[38] J. P. Perdew, A. Ruzsinszky, G. I. Csonka, L. A. Constantin, and J. Sun, Phys. Rev. Lett. **106**, 179902 (2011).

[39] S. Grimme, J. Antony, S. Ehrlich, and H. Krieg, J. Chem. Phys. **132**, 154104 (2010).

[40] S. Grimme, S. Ehrlich, and L. Goerigk, J. Comput. Chem. **32**, 1456 (2011).

[41] L. Goerigk, A. Hansen, C. Bauer, S. Ehrlich, A. Najibi, and S. Grimme, Phys. Chem. Chem. Phys. **19**, 32184 (2017).

[42] A. Patra, S. Jana, L. A. Constantin, and P. Samal, J. Chem. Phys. **153**, 084117 (2020).

[43] S. Ehlert, U. Huniar, J. Ning, J. W. Furness, J. Sun, A. D. Kaplan, J. P. Perdew, and J. G. Brandenburg, J. Chem. Phys. **154**, 061101 (2021).

[44] Minor deviations from the rocksalt structure were removed by symmetrization. This changed the energy by less than $3 \cdot 10^{-4}$ Hartree or less than $1\,\mathrm{kJ/mol}$. Typically, changes are below 10^{-5} Hartree.